Enhanced, mass-conserving closure scheme for lattice Boltzmann equation hydrodynamics



2006 J. Phys. A: Math. Gen. 39 10589

(http://iopscience.iop.org/0305-4470/39/33/024)

INSTITUTE OF PHYSICS PUBLISHING JOURNAL OF PHYSICS A: MATHEMATICAL AND GENERAL

J. Phys. A: Math. Gen. **39** (2006) 10589–10601 doi:10.1088/0305-4470/39/33/024

# Enhanced, mass-conserving closure scheme for lattice Boltzmann equation hydrodynamics

**A Hollis, I Halliday and C M Care**

Materials Research Institute, Sheffield Hallam University, Howard Street, S1 1WB, UK

Received 5 January 2006, in final form 1 June 2006
Published 2 August 2006
Online at stacks.iop.org/JPhysA/39/10589

**Abstract**

We derive and demonstrate a practical and accurate algorithm designed to impose Dirichlet boundary conditions (specified boundary velocity) on the edge nodes of a lattice Boltzmann fluid simulation space. The current algorithm models the lattice fluid on boundary and bulk nodes to identical accuracy and in a demonstrably equivalent manner. Whilst this new method applies to rectangular geometries, it adds to our previous method [2] (i) the condition of mass conservation and (ii) the ability to treat with unimpaired accuracy both internal and external corners.

PACS numbers: 47.11.Qr, 47.85.−g

## 1. Introduction

Accurate representation of boundary conditions is essential in all computational fluid dynamics. Here we derive, then demonstrate, a robust simulation lattice closure for one isothermal, single phase, two-dimensional lattice Boltzmann (lB) [1] method. Our readily adaptable approach evolves fluid at a boundary to the same accuracy as the bulk lB fluid and extends our previous technique [2] in two ways. First we shift emphasis from boundary pressure onto boundary mass conservation (necessary for multi-component applications) and, second, we enable the treatment of corner geometries with no diminution of accuracy. In these respects, our new method is as convenient as the popular lB strategy of mid-link bounce-back [1]; however it has additional advantages of (i) accuracy, (ii) imposing boundaries on a given lattice node (not e.g., at the mid-point between nodes), (iii) being instantaneously accurate and (iv) being capable of representing moving fluid boundaries, including boundaries crossed by fluid.

Solutions of the Navier–Stokes and continuity equations, $\mathbf{v}(\mathbf{r}, t)$, $P(\mathbf{r}, t)$, are most conveniently closed by Dirichlet boundary conditions on fluid velocity (only):

$$\mathbf{v}(\mathbf{r}, t)|_{\mathbf{r}'t} = \mathbf{u}_0(\mathbf{r}', t), \tag{1}$$

where $\mathbf{r}'$ denotes a position on the boundary of the flow domain and $\mathbf{u}_0(\mathbf{r}', t)$ is a specified boundary velocity distribution. The several lattice closure methods in lB [1] each amount to

  

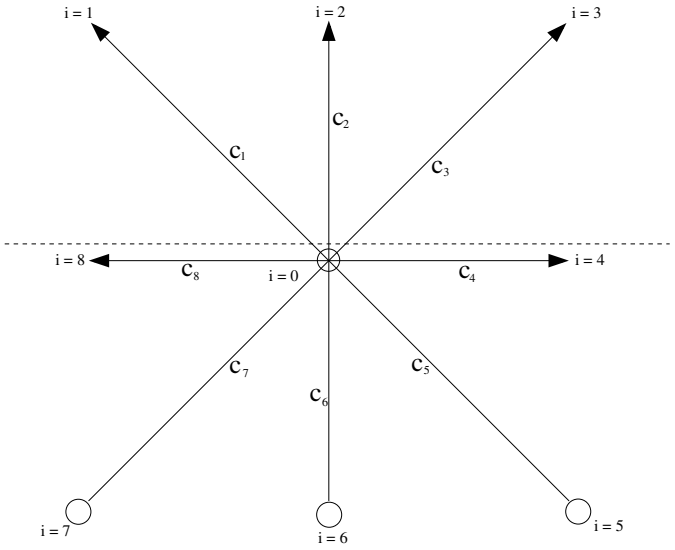


**Figure 1.** A boundary node on a horizontal wall, immediately prior to a collision step. Links $i = 1, 2, 3$ ($i = 0, 4, \ldots, 8$) all point into solid (fluid). The wall location is denoted by the dashed line. Propagated link data are denoted by an arrowhead on the link, lack of data by an open circle.

a means of imposing a given $\mathbf{u}_0(\mathbf{r}', t)$. Bounce-back has been carefully evaluated (at steady state, note) by a number of workers (e.g. [3, 4]) and He and Zou *et al* have shown how it is possible analytically to predict *boundary slip velocities* [5]. Later, more accurate lB boundary algorithms involve bouncing-back the non-equilibrium part of the lB momentum densities [6]; extrapolation [7]; the introduction of a counter-slip velocity [8]; second-order bounce-back [9] and Skordos [10] has solved the problem of boundary closure by deriving auxiliary partial differential equations which may be solved for lattice boundary information. Of some importance here is one of the most overlooked and most general approaches to simulation lattice closure—the locally second-order boundary method (LSOB) of Ginzbourg and d'Humières [11]. In a recent innovation, Ansumali and Karlin have developed a lB no-slip boundary condition from kinetic theory [12] and Sbragaglia and Succi have calculated slip flow resulting from boundary conditions based in kinetic theory [13].

In this paper, we derive, test bench and then evaluate a tractable, practical, simple-to-implement and portable closure step which is demonstrably equivalent to applying Dirichlet boundary conditions. Our method assumes a known boundary velocity and local mass conservation. It yields correct behaviour at every time step, represents boundary lattice fluid to the same accuracy as the bulk lattice fluid and it may be applied to immiscible fluids in contact at a boundary. We derive the method for a locally flat wall at which fluid is moving (with a specified velocity) in section 3.1; then summarize equivalent results for internal and external corners in section 3.2 and, briefly, comment on other cases in section 3.3. To evaluate and demonstrate our method we present accuracy plots based upon (exactly solved) duct flow and stream functions obtained from a square cross-section lid-driven cavity in section 4.

It is henceforth assumed that our lB boundary nodes lie infinitesimally *within* the lattice fluid, which, we again stress, is assumed to be moving at a specified velocity. We work in 2D, using the popular D2Q9 lattice (see figure 1). However, our analysis generalizes to 3D directly, by following the principal steps and analysis presented here. For consistency and simplicity we use, here, the notation and approach of our previous work [2].

## 2. Background

We take the two-dimensional, nine velocity D2Q9 LBGK model of Qian and d'Humières [14], analysed in detail by Hou *et al* [15]. Denote vectors of the velocity basis $\mathbf{c}_i$ and use the $i$-indexing of figure 1. Collision and propagation of lB's primary quantity, the link-based momentum distribution function $f_i(\mathbf{r}, t), i = 0, \ldots, 8$ is written as

$$f_i(\mathbf{r} + \mathbf{c}_i\delta_t, t + \delta_t) = f_i^{\dagger}(\mathbf{r}, t) = f_i(\mathbf{r}, t) + \frac{\delta_t}{\tau}\left(f_i^{(0)}(\rho, \mathbf{v}) - f_i(\mathbf{r}, t)\right) + t_p G, \tag{2}$$

where $\delta_t$ represents the time step; $\tau(>1/2)$ determines a lattice fluid viscosity:

$$\nu = \left(\frac{2\tau - 1}{6}\right)\frac{\Delta x}{\delta_t^2}, \tag{3}$$

$f_i^{\dagger}(\mathbf{r}, t)$ is the post-collision, pre-propagate value of the momentum density; $t_p G$ is a source term which may be used to represent a uniform pressure gradient [1, 16] or interfacial tension in the case of multiple immiscible fluids [1], $\Delta X$ is the lattice spacing and all other symbols have their usual meaning [14, 15]. Henceforth we shall set $\Delta X = \delta_t = 1$.

The macroscopic fluid density and momentum are defined by moments of the $f_i$'s:

$$\rho = \sum_i f_i, \qquad \rho\mathbf{v} = \sum_i f_i \mathbf{c}_i, \tag{4}$$

and the equilibrium distribution function, $f_i^{(0)}$, is [14, 15]

$$f_i^{(0)}(\rho, \mathbf{v}) = t_p \rho \left[1 + \frac{\mathbf{v}\cdot\mathbf{c}_i}{c_s^2} - \frac{v^2}{2c_s^2} + \frac{(\mathbf{v}\cdot\mathbf{c}_i)^2}{2c_s^4}\right]. \tag{5}$$

In equation (5), weight $t_p = 4/9, 1/9, 1/36$ for $i = 0$, $i$ even, $i$ odd respectively (figure 1); speed of sound $c_s = 1/\sqrt{3}$ for the D2Q9 lattice. The choice of $f_i^{(0)}$ given in equation (5) underwrites relations:

$$\rho = \sum_i f_i^{(0)}, \qquad \rho\mathbf{v} = \sum_i f_i^{(0)}\mathbf{c}_i, \tag{6}$$

and also the pressure tensor:

$$\Pi_{\alpha\beta}^{(0)} \equiv \frac{1}{3}\rho\delta_{\alpha\beta} + \rho v_\alpha v_\beta = \sum_i f_i^{(0)} c_{i\alpha} c_{i\beta}. \tag{7}$$

Higher order contributions to $f_i(\mathbf{r}, t)$, denoted by $f_i^{(n>0)}$, are introduced through the Chapman Enskog expansion [15]:

$$f_i = f_i^{(0)} + \delta_t f_i^{(1)} + \delta_t^2 f_i^{(2)} + \delta_t^3 f_i^{(3)} + \cdots \tag{8}$$

Equation (6) ensures that

$$\sum_i f_i^{(n)}\Delta_i = 0 \qquad n > 0, \tag{9}$$

where $\Delta_i = 1, c_{ix}, c_{iy}$. However, the second moments of the $f_i^{(n)}$ are not zero:

$$\sum_i f_i^{(1)} c_{i\alpha} c_{i\beta} = -2c_s^2 \rho\tau S_{\alpha\beta} \tag{10}$$

[17]. $S_{\alpha\beta}$ is the rate of strain tensor. Equations (9) and (10) provide six equations for the nine $f_i^{(1)}$'s. Note, by combining equations (8) and (2):

$$f_i^{\dagger}(\mathbf{r}, t) = f_i^{(0)}(\mathbf{r}, t) + \left[f_i^{(1)\dagger} \equiv \left(1 - \frac{1}{\tau}\right)\delta_t f_i^{(1)}\right] + o\left(\delta_t^2 f_i^{(2)}\right). \tag{11}$$

## 3. Mass-conserving lattice closure algorithm

Our previous method [2] allows a boundary pressure freely to develop; so boundary node density varies. In contrast, the present method conserves the density associated with what we designate *fluid* links (see below). This changed assumption raises key limitations in our original analysis and lends the resulting method to a wider range of geometries and situations (in particular, to wetting). In this section we shall treat planar and corner boundaries in separate subsections.

In terms of the lB method, our purpose may be summarized as follows. Momentum densities, $f_i$, to populate the links of a boundary node shall be constructed, subject to the requirements that they (the $f_i$'s) should (i) evolve according to rules demonstrably equivalent to those governing bulk nodes; (ii) are consistent with a known local velocity; (iii) conserve mass locally.

### *3.1. Flat boundary*

A plane 3D boundary containing the shortest lattice links is the analogue of the flat, 2D boundary considered in this section. As we shall indicate, the 2D case considered addresses all the issues which emerge when implementing the method in 3D.

All non-boundary nodes are assumed to be evolved according to (2). Figure 1 shows a boundary site on the D2Q9 lattice. The dotted line indicates the supposed uppermost extent of the lattice fluid. Links indexed $i = 1, 2, 3$ are cut by the boundary. At the end of a propagation step, a *pre-collision* value of lattice momentum density, $f_i$, exists for all links $i \neq 5, 6, 7$ (a situation represented by the use of empty circles in figure 1).

The boundary velocity provides two conditions on (moments of) the $f_i$'s, through equations (4), but there are three post-collision $f_i^\dagger$'s which need to be obtained, namely $f_5^\dagger$, $f_6^\dagger$ and $f_7^\dagger$ in the present case. Note that, in the analogous case of 3D, a boundary velocity provides three conditions on moments of the $f_i$'s; for the D3Q15 lattice five post-collision $f_i^\dagger$'s would be required; the essential problem of under-specification remains.

At a boundary node, links designated *live* require values of $f_i$ (links $i \neq 1, 2, 3$ in figure 1 are all live); these links connect to the flow domain and influence the subsequent evolution of adjacent nodes. The $f_i$'s on *dead* links are lost as they propagate into the boundary. For the geometry of figure 1, pre-collision $f_i$'s exist for links $i = 0, 1, 2, 3, 4, 8$ (some of which are dead, note), post-collision $f_i^\dagger$'s are required only for live links $i = 0, 4, 5, 6, 7, 8$.

Boundary mass conservation may only be defined in terms of equality between pre-collision and post-collision subtotals of the $f_i$'s and the $f_i^\dagger$'s. For the geometry of figure 1 local mass conservation may be expressed as

$$\left( M \equiv \sum_{i \neq 5,6,7} f_i \right) = \sum_{i \neq 1,2,3} f_i^\dagger . \tag{12}$$

For the remainder of the present subsection all equations and expressions apply to the particular geometry of figure 1. We proceed to construct a post-collision $f_i$, instantaneously correct to the accuracy of the bulk lB model $\left(o\left(f_i^{(1)}\right)\right)$, for all links $i = 0, \ldots, 8$, in the following principal steps:

(1) Determine a mass-conserving boundary node density, $\rho'$, and hence the $f_i^{(0)}(\rho', \mathbf{u_0})$, $i = 0, \ldots, 8$. *Effective* density $\rho'$ is calculated such that

$$\sum_{i \neq 5,6,7} f_i^{(0)}(\rho', \mathbf{u_0}) = M, \tag{13}$$

where $M$ is defined in equation (12).

(2) Determine pre-collision $f_i^{(1)}$'s which satisfy an under-specified system *after* equations (9) and (10).
(3) Collide and propagate the boundary sites according to equation (2).

Before expanding steps 1–3, it is necessary briefly to make three important points regarding the 'under-specified' system used for $f_i^{(1)}$'s. Still considering the $y =$ constant boundary in figure 1: (i) to conserve the total mass on (only) live links, we choose to modify the constraints on $f_i^{(1)}$'s as follows:

$$\sum_{i\neq 1,2,3} f_i^{(1)} = 0, \tag{14}$$

$$\sum_i f_i^{(1)} c_{i\alpha} = 0, \tag{15}$$

$$\sum_i f_i^{(1)} c_{i\alpha} c_{i\beta} = -\frac{2}{3}\rho'\tau S_{\alpha\beta}. \tag{16}$$

The corresponding post-collision values of $f_i^{(1)\dagger}$ are all clearly proportional (see equation (11)) to the solution of the system in equations (14)–(16). (ii) The condition of local boundary mass conservation is stated by equation (14). In treating a forced fluid at a boundary, particular care must be exercised around equation (14); see subsection 3.3. (iii) Equations (14)–(16) essentially characterize the 3D case of a flat boundary, the only modification necessary being the subscript range in equation (14), which, in the case of a 3D planar boundary on D3q15, needs to exclude the particular five cut links.

*Step 1*. Evaluate $M$ from the definition in equation (12). Since boundary velocity $\mathbf{u_0}$ is known, equations (5) and (13) provide an identity for effective density parameter $\rho'$:

$$\rho' = \frac{M}{\sum_{i\neq 1,2,3} t_p \left[1 + \frac{\mathbf{u_0}\cdot\mathbf{c}_i}{c_s^2} - \frac{u_0^2}{2c_s^2} + \frac{(\mathbf{u_0}\cdot\mathbf{c}_i)^2}{2c_s^4}\right]} = \frac{12M}{10 + 6u_{0y} - 6u_{0y}^2}. \tag{17}$$

It is now possible to assign $f_i^{(0)}(\rho', \mathbf{u_0})$. Note that over the entirety of links $i = 0, \ldots, 8$ at our boundary node, mass is not conserved. However, on links $i \neq 1, 2, 3$ there is a total mass $M$. The generalization of this step to 3D is transparent.

*Step 2*. Whilst the assumed boundary velocity, $\mathbf{u_0}$ and $\rho'$ uniquely determine $f_i^{(0)}$, strain rate $S_{\alpha\beta}$ is used to fix the $f_i^{(1)}$'s. The nine $f_i^{(1)}, i = 0, \ldots, 8$ satisfy the six equations (14)–(16) reproduced and re-formatted below, for convenience:

$$\begin{array}{rrrrrrrrrl}
f_0^{(1)} & +0f_1^{(1)} & +0f_2^{(1)} & +0f_3^{(1)} & +f_4^{(1)} & +f_5^{(1)} & +f_6^{(1)} & +f_7^{(1)} & +f_8^{(1)} & = 0, \\
 & -f_1^{(1)} & & +f_3^{(1)} & +f_4^{(1)} & +f_5^{(1)} & & -f_7^{(1)} & -f_8^{(1)} & = 0, \\
 & f_1^{(1)} & +f_2^{(1)} & +f_3^{(1)} & & -f_5^{(1)} & -f_6^{(1)} & -f_7^{(1)} & & = 0, \\
 & f_1^{(1)} & & +f_3^{(1)} & +f_4^{(1)} & +f_5^{(1)} & & +f_7^{(1)} & +f_8^{(1)} & = -2\rho\tau/3\ S_{xx}, \\
 & f_1^{(1)} & +f_2^{(1)} & +f_3^{(1)} & & +f_5^{(1)} & +f_6^{(1)} & +f_7^{(1)} & & = -2\rho\tau/3\ S_{yy}, \\
 & -f_1^{(1)} & & +f_3^{(1)} & & -f_5^{(1)} & & +f_7^{(1)} & & = -2\rho\tau/3\ S_{xy}.
\end{array} \tag{18}$$

Note that the terms in the first equation with coefficient 0 are removed from the equivalent system of equations in [2] by our altered assumptions. The strain rates in the last three equations were all measured using spatially $o(3)$ accurate finite differences. For the shadow

**Table 1.** Diagrammatic representation of the forbidden $f_i^{(1)}$ combinations for the planar boundary geometry of figure 1. The small (large) dot represents inclusion (exclusion) of the rest link.

| Forbidden set of three free $f_i^{(1)}$'s | Link representation |
|---|---|
| $f_1^{(1)}, f_2^{(1)}, f_3^{(1)}$ |  |
| $f_3^{(1)}, f_4^{(1)}, f_5^{(1)}$ |  |
| $f_5^{(1)}, f_6^{(1)}, f_7^{(1)}$ |  |
| $f_1^{(1)}, f_7^{(1)}, f_8^{(1)}$ |  |
| $f_0^{(1)}, f_4^{(1)}, f_8^{(1)}$ |  |

case of a 3D, D3Q15 planar boundary, the corresponding system would contain ten equations in 15 $f_i^{(1)}$'s.

To solve this under-determined system of equations (18), select a triplet of $f_i^{(1)}$'s as free variables, in terms of whose values the remaining six basic variables are to be found. Certain triplets of the free $f_i^{(1)}$'s are forbidden; this may be understood by temporarily re-defining quantities as follows:

$$\begin{aligned} g_1 &\equiv f_1^{(1)} + f_2^{(1)} + f_3^{(1)} \\ g_2 &\equiv f_5^{(1)} + f_6^{(1)} + f_7^{(1)} \\ g_3 &\equiv f_3^{(1)} + f_4^{(1)} + f_5^{(1)} \\ g_4 &\equiv f_1^{(1)} + f_7^{(1)} + f_8^{(1)} \\ g_5 &\equiv f_0^{(1)} + f_4^{(1)} + f_8^{(1)}, \end{aligned} \tag{19}$$

in terms of which $g_i$'s the first five of the six equations (18) become

$$\begin{aligned} &g_2 + g_5 = 0 \qquad g_3 - g_4 = 0 \qquad g_1 - g_2 = 0 \\ &g_3 + g_4 = -(2\rho\tau/3)S_{xx} \qquad g_1 + g_2 = -(2\rho\tau/3)S_{yy}. \end{aligned} \tag{20}$$

System (20) may be solved for the $g_1, \ldots, g_5$ in terms of the $S_{\alpha\beta}$. Clearly, a value for $g_1$ (say) constrains the three $f_i^{(1)}$'s contained in its definition, $f_1^{(1)}$, $f_2^{(1)}$ and $f_3^{(1)}$, to a particular sum. Several forbidden triplets of free $f_i^{(1)}$'s arise in this way; their elements are defined in table 1 alongside a diagrammatic interpretation. Note, the sixth equation in the system (18) cannot be expressed in terms of $g_1, \ldots, g_5$ (scrutiny of the second column in table 1 demonstrates this) and so does not yield relevant information.

The planar D3Q15 boundary would be subject to equivalent considerations; forbidden quintuplets of $f_i^{(1)}$'s now occur in precisely analogous ways.

In addition to the structure of system (20), the set of $f_i^{(1)}$'s selected as free variables should depend upon which directions $\mathbf{c_i}$ contain pre-collision information originating in the

flow domain. Therefore, in order to solve the system of equations (14)–(16), choose free $f_i^{(1)}$'s which (i) are not a forbidden set *and* (ii) have accessible values. Criterion (ii) requires that one must select $f^{(1)}$'s corresponding to defined pre-collision $f_i$'s; The third row in table 1 corresponds to a set of $f_i^{(1)}$'s each of which originates outside the boundary. Here pre-collision values of $f_i^{(1)} \approx f_i - f_i^{(0)}$, $i = 0, 1, 2$, were chosen, making the following solution for the particular boundary case represented in figure 1:

$$\begin{aligned}
f_3^{(1)} &= -\kappa S_{yy} - f_1^{(1)} - f_2^{(1)},\\
f_4^{(1)} &= -\kappa S_{xy} + \tfrac{3}{2}\kappa S_{yy} - \tfrac{1}{2} f_0^{(1)} + 2 f_1^{(1)} + f_2^{(1)},\\
f_5^{(1)} &= -\tfrac{1}{2}\kappa (S_{xx} + S_{yy}) - \tfrac{1}{2}\kappa S_{xx}\kappa S_{xy} + \tfrac{1}{2} f_0^{(1)} - f_1^{(1)} = -\tfrac{1}{2}\kappa S_{xx}\kappa S_{xy} + \tfrac{1}{2} f_0^{(1)} - f_1^{(1)},\\
f_6^{(1)} &= 3\kappa S_{xx} - f_0^{(1)} - f_2^{(1)},\\
f_7^{(1)} &= -\tfrac{1}{2}\kappa S_{xx} - \kappa S_{xy} + \tfrac{1}{2} f_0^{(1)} + f_1^{(1)} + f_2^{(1)},\\
f_8^{(1)} &= -\tfrac{1}{2}\kappa S_{yy}\kappa S_{xy} - \tfrac{1}{2} f_0^{(1)} - 2 f_1^{(1)} - f_2^{(1)}
\end{aligned} \tag{21}$$

where $\kappa \equiv c_s^2 \rho \tau$. Similar considerations to those imposed to arrive at the above solution would apply to the 3D, D3Q15 planar boundary.

*Step 3*. The pre-collision boundary node $f_i^{(1)}$'s constructed in step 2 are collided, using equation (11), then added to the corresponding $f_i^{(0)}(\rho', \mathbf{u_0})$, yielding a post-collision momentum density:

$$f_i^{\dagger}(\mathbf{r}, t) = f_i^{(0)}(\rho', \mathbf{u_0}) + \left(1 - \frac{1}{\tau}\right) f_i^{(1)}. \tag{22}$$

Propagation completes the evolution of our boundary site. Step 3 generalizes to 3D without modification.

### *3.2. Internal and external corners*

It is an advantage to be able to treat internal and external corners with the method outlined in section 3.1.

*Internal corner.* Figure 2 shows a top-left internal corner boundary node. The dotted line shows the supposed location of the boundary. Quantities $f_3$, $f_7$ (links represented by broken lines) are ghost (not, note, dead) quantities which never participate. $f_0^{\dagger}$, $f_4^{\dagger}$, $f_5^{\dagger}$ and $f_6^{\dagger}$ are required. For the geometry of figure 2 the appropriate value of $M$ is

$$M \equiv \sum_{i \neq 3,4,5,6,7} f_i, \tag{23}$$

and the value of $\rho'$ is therefore

$$\begin{aligned}
\rho' &= \frac{M}{\sum_{i \neq 1,2,3,7,8} t_p \left[1 + \frac{\mathbf{u_0}\cdot\mathbf{c}_i}{c_s^2} - \frac{u_0^2}{2c_s^2} + \frac{(\mathbf{u_0}\cdot\mathbf{c}_i)^2}{2c_s^4}\right]},\\
&= \frac{36M}{25 - 15u_{0x} + 15u_{0y} - 9u_{0x}u_{0y} - 15u_{0x}^2 - 15u_{0y}^2}.
\end{aligned} \tag{24}$$

The last expression for $\rho'$ has complicated dependence upon $\mathbf{u_0}$. However, this does not appear to affect the stability of the resulting scheme. Neither does the fact that the denominator can vanish for $u_0 \approx 1$, as this value of velocity violates the usual restriction $u_0 < 0.1$.

The mass-conservation condition corresponding to equation (14) for this geometry is

$$\sum_{i \neq 1,2,3,7,8} f_i^{(1)} = 0. \tag{25}$$

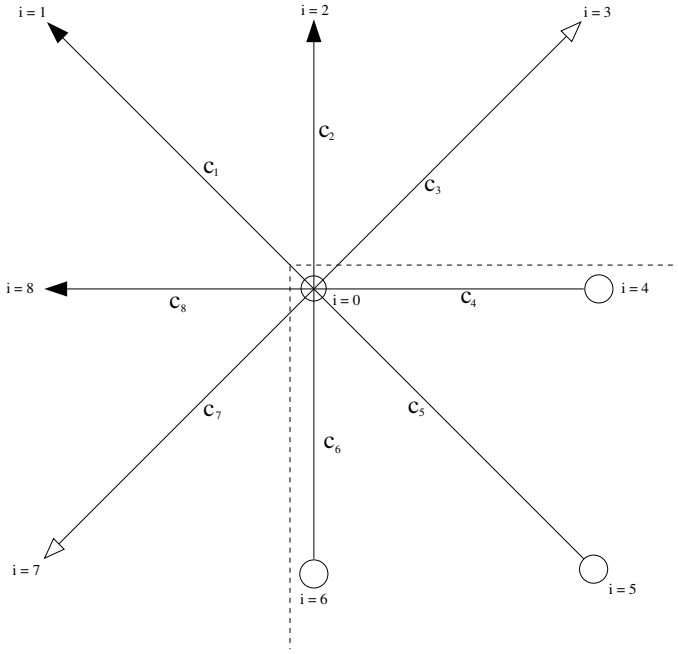


**Figure 2.** A boundary node on an internal corner. The walls locations are denoted by the dashed lines. The node is taken to lie in the fluid with the rest link. Propagated link data are denoted by a solid arrowhead or solid square on the link, unavailable link information (lack of data) by an open circle. Ghost links, which never participate, are indicated by open arrowheads.

Solving for pre-collision $f_i^{(1)}$'s now follows the procedure in section 3.1. No triplets of *obtainable* $f_i^{(1)}$'s arise for the internal corner geometry.

*External corner.* Figure 3 shows a top-left external corner. The dotted line shows the supposed location of the boundary. $f_0^\dagger$, $f_1^\dagger$, $f_2^\dagger$, $f_3^\dagger$, $f_4^\dagger$, $f_5^\dagger$, $f_6^\dagger$ and $f_8^\dagger$ are required. For $M$ and $\rho'$ we now have

$$M = \sum_{i \neq 1} f_i, \tag{26}$$

and

$$\begin{aligned} \rho' &= \frac{M}{\sum_{i\neq 3} t_p \left[1 + \frac{\mathbf{u_0}\cdot\mathbf{c}_i}{c_s^2} - \frac{u_0^2}{2c_s^2} + \frac{(\mathbf{u_0}\cdot\mathbf{c}_i)^2}{2c_s^4}\right]}, \\ &= \frac{36M}{35 + 3u_{0x} - 3u_{0y} - 3u_{0x}^2 + 9u_{0x}u_{0y} - 3u_{0y}^2}. \end{aligned} \tag{27}$$

The mass-conservation condition corresponding to equation (14) for this geometry is

$$\sum_{i \neq 5} f_i^{(1)} = 0. \tag{28}$$

Solving for pre-collision $f_i^{(1)}$'s again follows the procedure in section 3.1. Triplets of evaluatable $f_i^{(1)}$'s now forbidden are listed in table 2.

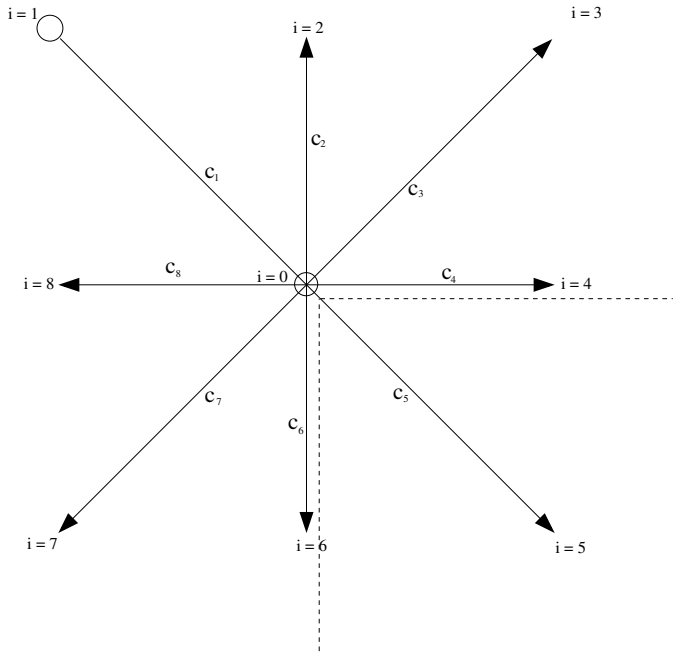


**Figure 3.** A boundary node on an external corner. The walls locations are denoted by the dashed lines; the node is taken to lie in the fluid. Propagated link data are denoted by a solid arrowhead or solid square on the link, unavailable link information (lack of data) by an open circle.

**Table 2.** Diagrammatic representation of the forbidden combinations of $f_i^{(1)}$'s as free variables, for the external corner geometry of figure 3. Note that a large dot indicates inclusion of the rest link. Note also that, unlike table 1, only triplets which contain evaluatable $f_i^{(1)}$'s are listed here.

| Forbidden set of three free $f_i^{(1)}$'s | Link representation |
|---|---|
| $f_0^{(1)}, f_6^{(1)}, f_7^{(1)}$ | |
| $f_0^{(1)}, f_4^{(1)}, f_3^{(1)}$ | |

### *3.3. Other cases: forces close to the boundary*

Clearly other geometries and other situations are amenable to the boundary analysis of this section. Situations in 3D, corresponding to any number of cut links are a straightforward generalization of current method. Further extension to off-lattice boundaries is more complicated but it requires no fundamental modification to the method; the process will be fully reported elsewhere, in context of Lagrangian particles. The situation encountered when considering multiple immiscible fluids does, however, merit further comment.

All immiscible lattice Boltzmann fluids have interfaces supported by segregating forces impressed between different fluids. The forcing applied generally conserves mass over all lattice links $\mathbf{c_i}$, and is represented by an appropriate choice of source term $t_p G$ in equation (2). For lattice fluid interfaces at a boundary (the wetting problem), it is therefore

necessary to apply a segregating force to fluids at boundary fluid node. This force will not, in general, conserve mass on only the uncut links. Accordingly, it is necessary to re-state our mass-conservation condition (equation (14) for the planar boundary) to apply *post-collision*. The essential extension of our boundary method to the wetting problem involves (i) redefinition of the $f^{(i)}$'s to contain the source terms $t_p G$ in equation (2) and (ii) applying the mass-conservation constraint to post-collision $f_i^{(i)\dagger}$'s. So, for the planar boundary of figure 3, equation (14) is replaced:

$$\sum_{i\neq 1,2,3} \left(f_i^{(1)\dagger} + t_p G\right) = 0. \tag{29}$$

In fact the presence of a source term requires corrections in equation (10) [18] which complicates solution of the wetting problem.

## 4. Results

To demonstrate that our boundary closure is robust, to verify its time resolution and to show that it accommodates moving boundaries we considered a lattice fluid initially at rest ($f_i(\mathbf{r}, 0) = f_i^{(0)}(\rho, \mathbf{0})$ everywhere) between two horizontal planar boundaries $y = 0^-, W^+$; the latter was impulsively started from rest at $t = 0^+$ to velocity $(u_0, 0)$. The analytic solution to this transient flow is

$$v_x(y,t) = \frac{u_0}{W}y + \frac{2u_0}{\pi}\sum_m \frac{(-1)^m}{m}\sin\left(\frac{m\pi y}{W}\right) \times \mathrm{e}^{-m^2\pi^2\bar{t}}, \qquad \bar{t} = \frac{\nu t}{W^2}. \tag{30}$$

Here $\bar{t}$ represents a *dimensionless* time parameter. Snapshots of the developing flow across the whole width of the duct, obtained for discrete times $t = 10, 100, 1000$ with collision parameter, $1/\tau = 0.6, 1.0, 1.6$, were collected. Results with the present method are identical to those presented elsewhere [2]; our earlier remarks [2] apply.

To make comparison with the popular and robust methods of on-link and mid-link bounce-back boundary conditions, steady-state duct flow was simulated. This requires $\mathbf{u_0} = \mathbf{0}$. Planar boundaries, taken to be parallel to the $x$-direction, were represented by (a) on-link bounce-back boundary conditions (b) mid-link bounce back and (c) the method of section 3.1; periodic boundary conditions were used in the $y$-direction. Flow rate and hence Reynolds' number, $Re$, was fixed by the constant parameter $G$ in equation (2). Note that $G = 0$ on the boundaries. The corresponding analytical solution is

$$\left(v_0(y) \equiv \frac{G}{6\rho\nu}y(W-y), 0\right). \tag{31}$$

The scalar difference between the measured steady-state flow profile, $(v_m(y), 0)$:

$$\Delta_W \equiv \sum_{y\neq 0} |v_m(y) - v_0(y)|, \tag{32}$$

was measured at constant $Re = 0.5$ for a range of lattice resolutions. The latter was parameterized by the duct width $W = 10 \times 2^N$, $N \leqslant 5$.

The data of figure 4 show the value of $\Delta_W$ as a function of resolution for boundary methods (a)–(c). The shortcomings of the first-order accurate 'on-link' bounce-back technique (a) in terms of the reduced accuracy of the solution close to the boundaries are documented elsewhere [2]. Mid-link bounce-back (b) and the method of section 3.1 (c) are both seen to be second-order accurate in spatial gradient (from the gradient in figure 4), with the latter slightly more accurate and, of course, capable of representing a boundary with any instantaneous velocity $|\mathbf{u_0}| < 0.1$.

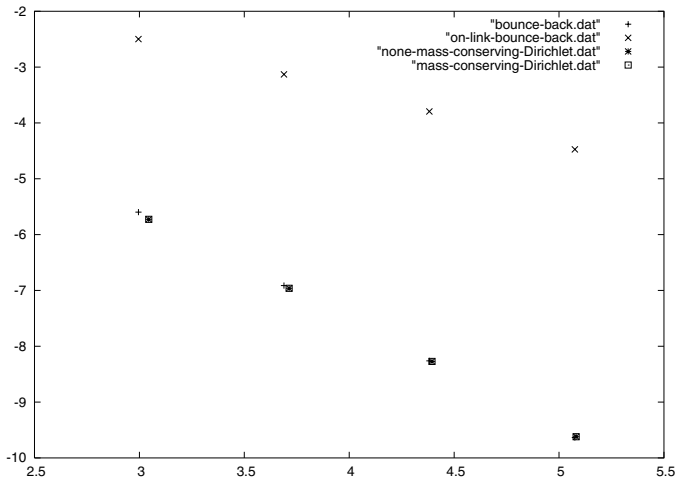


**Figure 4.** Error, $\Delta W$, defined in equation (32), as a function of lattice resolution. The latter is measured by lattice width $W$. $Re = 0.5$. These data represent (i) bounce-back, (ii) mid-link bounce-back, (iii) our non-mass-conserving method and (iv) our current mass-conserving boundary conditions. 3.1.

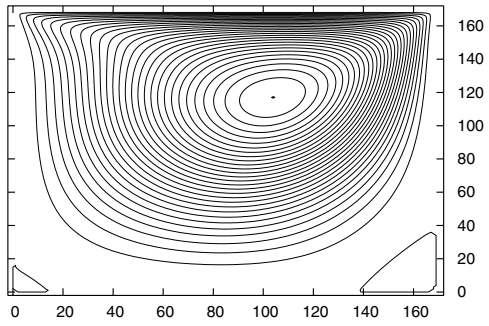


**Figure 5.** Steady-state stream function for a 2D square lid-driven cavity. Data correspond to a square box $170 \times 170$. The single relaxation parameter was $\tau = 0.77$; the density parameter $\rho = 1.8$. For the data shown $Re \sim 100$. The four internal corners and the planar boundaries were simulated using the method of section 3.1; corners in contact with the moving (top) lid were moved with the lid velocity. The cavity boundaries correspond to $x = 0, 170$, $y = 0, 170$; the slightly enlarged plot area facilitates resolution of the stream function's corner features.

In respect of figure 4, we note that mid-link bounce-back actually appears to perform well. However, the discussion below indicates that caution should be exercised in attributing second-order accuracy to mid-link bounce back.

In fact the errors calculated in figure 4 represent mid-link bounce-back in its most favourable light. Recall that the mid-link bounce-back lattice closure produces a no-slip boundary off-lattice. Its error (from equation (32)) allowed (a) for channel width variation and (b) departure of the measured $Re$ from that predicted. In respect of (a), an effective channel width was calculated from a $v_0(y)$ distribution obtained by extrapolating a parabola fitted to the bulk lattice positions' measured velocity. Also, the mid-link bounce-back nodes themselves were not included in the summation of equation (32). The uncertainty in the

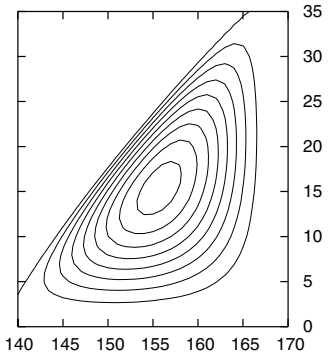


**Figure 6.** Detail of the steady-state stream function for a 2D square lid-driven cavity, shown in figure 5. This image corresponds to the weak, detached flow in the secondary vortex encountered in the bottom-right corner of the cavity.

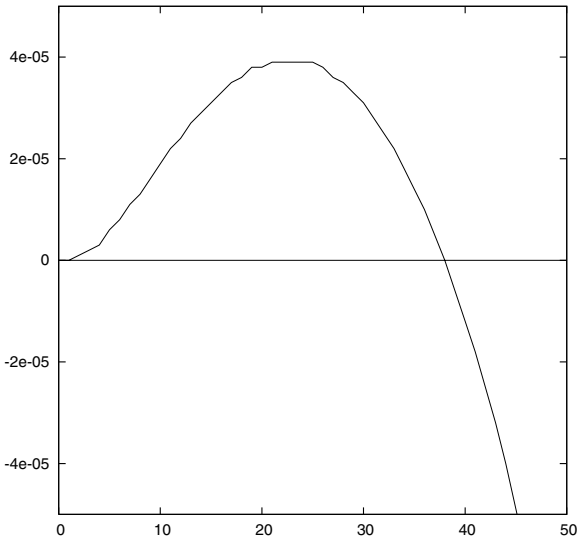


**Figure 7.** The $y$-velocity distribution along a vertical line $x = 169$, close to right-hand $x = 170$ boundary of the lid-driven cavity flow depicted in figures 5 and 6; the change in the sign of the $y$ velocity corresponds to the point in which the stream function detaches.

channel width was thus effectively ignored, as was the associated variation in the channel total discharge. Neglecting artefacts of the mid-link bounce-back method means that the measured *Re* differs from that predicted. By considering a parabolic profile, $v_0(y)$, corresponding to the *Re* predicted (on the basis of the channel pressure gradient, $G$) and considering all nodes, the error associated with mid-link bounce-back increases at all resolutions $W$ and reduces more slowly as $W$ increases. Under similar conditions, the error associated with the present method remains as indicated in figure 4. It is nevertheless interesting to note that, by compensating for its artefacts, the accuracy of the mid-link bounce-back method is promoted from the widely quoted $o(1.5)$ to second order.

To assess the accuracy of the corner boundaries of subsection 3.2, a square, 2D lid-driven cavity was simulated over a small range of $Re \approx 93$ (where a secondary vortex is known first

to appear) and resolutions. See figure 5 caption for simulation data. Figure 5 shows the stream function obtained with our new boundary conditions enforced over the entire boundary; in particular, the top corners of the enclosure were assumed to be moving with the lid speed. Figure 6 shows detail of the stream function in the bottom-right corner of the flow. Figure 7 shows the $y$-component of velocity along the right-hand boundary; the point of detachment is clearly visible in these data.

## 5. Conclusion

We have set out and validated a very adaptable method for closing a lattice Boltzmann simulation lattice by calculating appropriate values for the set of 'missing' momentum densities, subject to the condition of local mass conservation. Like our previous algorithm, which allowed pressure adaptation at the boundary [2], the current method is demonstrably accurate, flexible and instantaneously correct. However, the present method can also apply (i) to an increased range of geometries other than the set presented here and (ii) to boundaries where fluid forces need to be impressed—in particular, the case of immiscible fluid–fluid interfaces at a boundary.

## References


[1] Succi S 2001 *The Lattice Boltzmann Equation for Fluid Mechanics and Beyond* (Oxford: Clarendon)
[2] Halliday I, Hammond L A and Care C M 2002 *J Phys A: Math. Gen.* **35** L157
[3] Gallivan M A, Noble D R, Georgiadis J G and Buckius R O 1997 *Int. J. Numer. Methods Fluids* **25** 249
[4] Noble D R, Chen S, Georgiadis J G and Buckius R O 1995 *Phys. Fluids* **7** 203
[5] He X Y, Zou Q, Luo L S and Dembo M 1997 *J. Stat. Phys.* **87** 115
[6] Zou Q and He X 1997 *Phys. Fluids* **9** 1591
[7] Chen S, Martinez D and Mei R 1996 *Phys. Fluids* **8** 2527
[8] Inamuro T, Yoshino M and Ogino F 1995 *Phys. Fluids* **7** 2928
[9] Kim I C 2000 *KSME Int. J.* **14** 84
[10] Skordos P A 1993 *Phys. Rev.* E **48** 4823
[11] Ginzbourg I and d'Humières D 1996 *J. Stat. Phys.* **84** 927
[12] Ansumali S and Karlin I V 2002 *Phys. Rev.* E **66** 026311
[13] Sbragaglia M and Succi S 2005 *Phys. Fluids* **17** 093602
[14] Qian Y H, d'Humières D and Lallemand P 1992 *Europhys. Lett.* **17** 479
[15] Hou S, Zou Q, Chen S, Doolen G D and Cogley A C 1995 *J. Stat. Phys.* **118** 329
[16] Halliday I, Hammond L A, Care C M, Good K and Stevens A 2001 *Phys. Rev.* E **64** 011208
[17] Zou Q and He X Y 1997 *Phys. Fluids* **9** 1591
[18] Halliday I, Law R and Care C M 2006 *Phys. Rev.* E in press
[19] Zou Q, Hou S, Chen S and Doolen G D 1995 *J. Stat. Phys.* **81** 319